Neuroimage: Reports 1 (2021) 100035

Contents lists available at ScienceDirect

Neuroimage: Reports

journal homepage: www.sciencedirect.com/journal/neuroimage-reports

The Laplacian eigenmaps dimensionality reduction of fMRI data for discovering stimulus-induced changes in the resting-state brain activity

Nikita Pospelov [a,*], Alina Tetereva [b,c], Olga Martynova [b], Konstantin Anokhin [a]

[a] Institute for Advanced Brain Studies, Lomonosov Moscow State University, Moscow, Russia
[b] Institute of Higher Nervous Activity and Neurophysiology of the Russian Academy of Science, Russia
[c] Department of Psychology, University of Otago, Dunedin, New Zealand

ARTICLE INFO

Keywords:
Resting-state fMRI
BOLD signal
Conditioned fear
Dimensionality reduction
Laplacian eigenmaps
Multiresolution analysis

ABSTRACT

The brain at wakefulness is active even in the absence of goal-directed behavior or salient stimuli. However, patterns of this resting-state (RS) activity can undergo long-term alterations following exposure to preceding meaningful stimuli. This study was aimed to develop an unbiased method to detect such changes in the RS activity after exposure to emotionally meaningful stimuli. For this purpose, we used functional magnetic resonance imaging (fMRI) of RS brain activity before and after acquisition and extinction of experimental conditioned fear. A group of healthy volunteers participated in three fMRI sessions: a RS before fear conditioning, a fear extinction session, and a RS immediately after fear extinction. The fear-conditioning paradigm consisted of three neutral visual stimuli paired with a partial reinforcement by a mild electric current. We used both linear and non-linear dimensionality reduction approaches to distinguish between the initial RS and the RS after stimuli exposure. The principal component analysis (PCA) as a linear dimensionality reduction method showed significantly worse results than non-linear methods (Isomap, LLE, Laplacian eigenmaps). Using the Laplacian eigenmaps manifold learning method, we were able to show significant differences between the two RSs at the level of individual participants. This detection was further improved by smoothing the BOLD signal with the wavelet multiresolution analysis. The developed method can improve the discrimination of functional states collected in longitudinal fMRI studies.

1. Introduction

The global brain dynamics generated at rest results in many superimposed patterns of activity known as resting-state networks (RSNs). RSNs are reproducible in the large samples of healthy subjects (van den Heuvel and Hulshoff Pol, 2010; Martynova et al., 2017) and are significantly altered in neurological and psychiatric disorders (Hohenfeld et al., 2018; Sheffield and Barch, 2016). The large-sample assessment of brain resting-state (RS) activity showed more robust results than task-induced fMRI, implying that RS functional connections could serve as biomarkers of brain disorders (Satterthwaite and Baker, 2015; Barch, 2017). Thus, RS activity is crucial for understanding the brain activity's dynamics and organization in health and disease.

Though RSNs are defined based on the absence of goal-directed behavior or salient stimuli, an important question is whether their activity reflects possible residual changes in rest after preceding task-induced activity. This question is especially relevant for understanding the mechanisms of anxiety and post-traumatic stress disorders (PTSD) (Graham and Milad, 2011). Indeed, several fMRI studies showed increased functional connectivity (FC) of some areas in RS after fear conditioning (Hahn et al., 2011; Prater et al., 2013; Baeken et al., 2014; Rus et al., 2017; Jung et al., 2018). RS fMRI data indicate a high correlation between anxiety and changes in FC (Kim et al., 2011; Belleau et al., 2018), as well as an increased FC in patients with PTSD between brain regions that are key for processing emotional stimuli (Zhou et al., 2012), even years after the stress exposure (Brown et al., 2014).

However, the high dimensionality of the fMRI data complicates their conventional analysis based on statistical parametric mapping (Fristen et al., 1996) of changes in the level of blood oxygenation dependent signal (BOLD) (Poldrack et al., 2008). The high dimensionality is especially problematic in the absence of an initial hypothesis that reduces dimensionality by focusing only on regions of interest.

Moreover, in conditions of the high dimensionality of data, valuable results may be lost due to the correction for multiple comparisons in the

* Corresponding author. Institute for Advanced Brain Studies, Lomonosov Moscow State University, Lomonosovsky av. 27, 119192, Moscow, Russia.
E-mail address: pospelov.na14@physics.msu.ru (N. Pospelov).

https://doi.org/10.1016/j.ynirp.2021.100035
Received 9 December 2020; Received in revised form 17 June 2021; Accepted 8 July 2021
Available online 13 July 2021

absence of pre-selected regions of interest. The loss of potential markers is especially crucial when comparing individual longitudinal data or comparing small samples of data in rare clinical diseases. Besides, personalized approaches come to the fore in clinical neuroscience, as it becomes essential to reveal the differences in the activity of the individual's brain rather than the statistical difference between groups to clarify the diagnosis, the effectiveness of treatment, and rehabilitation. From this point of view, data dimensionality reduction techniques could improve the efficiency of discriminating and classifying brain activity changes at both the individual and group levels, especially in the case of a data-driven approach.

It is believed that almost any high-dimensional data can be effectively nested in the space of significantly lower dimensionality - the so-called intrinsic manifold. When searching for such an internal space, it is usually assumed that there is no a priori data on the positions of points on the intrinsic manifold, that is, the data are unlabeled. The manifold learning methods are designed specifically to analyze this low-dimensional data structure.

Diffusion maps is an algorithm designed to map the data into a space in which the Euclidean distance between two points depends on the probability of getting from one to the other through a diffusion process in the original space (Coifman and Lafon, 2006). It has been successfully used to find the separation between the activated manifold and the background time series in event-related fMRI (Shen and Meyer, 2005).

The Laplacian eigenmaps (LE) method (Belkin and Niyogi, 2003) is a tool based on the clustering-related properties of graph Laplacian. It has been used to cluster and classify neuronal activity (Sun et al., 2019; Rubin et al., 2019) and applied to fMRI data to highlight areas of interest (Thirion and Faugeras, 2004), improve the accuracy of functional network discrimination (Liu et al., 2018), analyze fMRI data using diffusion-based spatial priors (Harrison et al., 2008) and classify brain activity in Alzheimer's disease (Hu et al., 2016).

Isomap (Tenenbaum et al., 2000) is a hybrid method which utilizes the graph-based approach and applies multidimensional scaling (MDS) on a matrix of geodesic graph distances between points in the initial space. In context of fMRI data it has been applied to classifying brain maps between groups of schizophrenic and healthy patients from fMRI scans during a resting-state experiment (Gallos and Siettos, 2017) and to produce low-dimensional embeddings of the correlation matrices for the parcellated time series (Gallos et al., 2021).

Locally linear embedding (LLE) is another classical manifold learning algorithm designed for finding an embedding of lower dimensionality that preserves local relationships between data points. It has proven itself to be effective in extracting informative measures of the underlying neuronal activity from BOLD time-series (Sidhu, 2019) and for separating non-linearly modulated activation sources in fMRI data in a low-dimensional subspace (Mannfolk et al., 2010).

Finally, modern dimensionality reduction methods, such as t-SNE (Van Der Maaten and Hinton, 2008) and UMAP (McInnes et al., 2018), are based on optimization of some error functional using gradient descent. These methods have proven to be excellent in practice but require large amounts of data and fine-tuned parameters.

A thorough investigation of machine learning methods in application to resting-state fMRI data can be found in the review of Khosla et al. (2019)

In this study, we examined the efficiency of the named nonlinear manifold learning methods (Isomap, LE and LLE) compared to the linear dimensionality reduction approach via PCA in revealing stimulus-dependent changes in the resting-state brain activity before and immediately after fear conditioning and fear extinction in healthy volunteers (Martynova et al., 2020).

2. Methods

2.1. Participants and procedure

We analyzed resting-state fMRI data of 23 healthy right-handed volunteers (23.90 ± 3.93 years old, 8 females) who participated in the study of longitudinal changes in the brain RS functional connectivity such as RS after fear learning and fear memory extinction (RS_FE) in comparison with the initial RS data (RS_0). These data were obtained in the previous study (Tetereva et al., 2020).

2.2. Ethical statement

The study's protocol followed the Helsinki Declaration's requirements, and the Ethics Committee of the Institute of Higher Nervous Activity and Neurophysiology of the Russian Academy of Science approved the study. All participants provided written, informed consent before the study.

2.3. Procedure description

The study procedure was as follows: 1) initial resting-state (RS_0) scanning; 2) procedure of fear learning (FL) out of scanner (Pavlovian fear conditioning); 3) fear extinction (FE), and 4) resting-state (RS_FE) scanning after fear extinction. The time between the RS_0 and RS_FE scans was approximately 45 min and between the FE and RS_FE, 1–2 min. During the RS scanning, participants were asked to remain calm with their eyes closed and to try not to think purposefully. A full description of the experimental procedure can be found in our previous paper (Tetereva et al., 2020). In the current study, we concentrated on analyzing RS1 and RS2 interleaved by FL and FE to separate two RS scan data acquired before and after exposure to emotionally meaningful stimuli.

2.4. Fear learning and fear extinction

The procedure of FL was conducted in a separate room in the behavioral laboratory. The FL consisted of two pseudo-random sequences with a short break between them. For FL, we used a delayed fear-conditioning paradigm with partial negative reinforcement. Three visual (geometric figures) conditioned stimuli were presented. One type of stimuli was always neutral. The presentation of each conditioned stimulus was followed by a white screen for a random duration of 8–12 s with a jitter of 2 s. The other 2 stimuli had the reinforcement probabilities of 70% and 30%, respectively. The unconditional stimulus was mild electrical current stimulation for 500 ms, which was presented immediately after the figure when a white screen appeared. The strength of the stimulation was selected individually to be a tolerable but painful stimulus. Before each stimulus, participants saw a fixation cross lasting 2 s. The duration of each conditional stimulus varied randomly from 4 to 8 s with a jitter of 2 s.

The second sequence was the same as the first, except that the probabilities of reinforcement for the conditioned stimuli were changed by 30% and 70%, respectively. The total duration of each FL block was 8 min 54 s.

During the FE session, the same stimuli were presented, but in a different pseudo-random order and with a more-extended overall sequence (10 min) and without US. During FE session, volunteers were asked to expect the unconditional stimulus, but with a different reinforcement rule than in the previous two sessions.

2.5. fMRI data acquisition

The MRI data were collected from the National Research Center Kurchatov Institute (Moscow, Russia) using a 3T scanner (Magnetom Verio, Siemens, Germany) equipped with a 32-channel head coil. The

anatomical images were collected using a T1-MPRAGE sequence: TR 1470 ms, TE 1.76 ms, FA 9°; 176 slices with a slice thickness of 1 mm, a slice gap of 0.5 mm, and a 320-mm field of view (FoV) with a matrix size of 320 × 320. Functional images (300 vol) were collected using a T2*-weighted echo-planar imaging (EPI) sequence having a GRAPPA acceleration factor equal to 4 and the following sequence parameters: TR 2000 ms, TE 20 ms, FA 90°; 42 slices acquired in interleaved order and having a slice thickness of 2 mm, a slice gap of 0.6 mm, and a 200-mm FoV with an acquisition matrix of 98 × 98. Besides, to reduce the EPI's spatial distortion, the magnitude and phase images were acquired using a field-map algorithm that had the following parameters: TR 468 ms, TE1 4.92 ms, TE2 7.38 ms, an FA 60°, 42 slices, and a 200-mm FOV. The scanner parameters for the RS_0, and RS_FE were the same, with equal session durations of 10 min.

2.6. fMRI data preprocessing

The data of both RS sessions were processed using MELODIC, a part of FSL (FMRIB's Software Library). We applied the following preprocessing steps: motion correction (MCFLIRT), slice-timing correction using Fourier-space time-series phase-shifting, non-brain removal (BET), spatial smoothing using a Gaussian kernel of FWHM 5 mm, grand-mean intensity normalization of the entire 4D dataset using a single multiplicative factor, high-pass temporal filtering with a removing of the linear trends (Gaussian-weighted, least-squares, straight-line fitting, with sigma = 50.0 s, which equals a cutoff of 0.01 Hz) (Jenkinson et al., 2002). The B0-distortion was removed during the inserted B0-unwrapping algorithm. Registration of functional images to the individual anatomical and standard space MNI152 mm3 was conducted using FLIRT (Jenkinson et al., 2002). Independent component analysis (ICA) was performed using probabilistic ICA as implemented in MELODIC (v 3.14). For each participant fMRI signal, 38 independent components were extracted. Next, additional denoising of the data was conducted using FIX v1.068 FMRIB's ICA-based Xnoiseifier (Griffanti et al., 2014) and ICA-based automatic removal of motion artifacts (ICA-AROMA) (Pruim et al., 2015). First, the AROMA was applied to 15 datasets (five randomly chosen from each RS_0 and RS_FE) in the classification regime to detect motion-related components. The results were then visually inspected to detect additional artifact components, including cerebrospinal fluid (CSF) pulsation in the ventricles. Second, FIX was trained based on the preliminarily classified 15 datasets, and new automatic classification was applied to the remaining 54 sets (23 participants 3 scanning sessions) to detect noisy components, which were filtered out using FIX cleanup mode with the option to clean up the motion confounds (24 regressors). There were no significant within-subject differences in the number of removed components between sessions (mean 19.4 ± 5.06 ICs). Finally, the cleaned data were subjected to filtering to resting-state frequencies of 0.01–0.1 Hz using the "3dTproject" AFNI algorithm.

2.7. Brain parcellation for obtaining BOLD signal

We extracted BOLD signal time series averaged from 245 parcells of the functional resting-state Brainnetom (BN) Atlas (Fan et al., 2016). We excluded the BN region 94 from the analysis as this region was absent in some individuals who had brain sizes larger than the used field of view. Each mask was converted to individual subject space using FLIRT FSL.

2.8. Analysis framework

Our main approach was to reduce the dimensionality of the data from the number of parcels to an effective one. The value of the BOLD signal indirectly depends on neurons' activity in the brain structure of interest (Region of Interest - ROI) (Poldrack et al., 2008). If we consider the BOLD response in a single ROI as a separate variable, the brain state at each moment can be represented as an $\boldsymbol{D}$-dimensional activity vector, where $\boldsymbol{D}$ corresponds to the number of investigated ROIs and depends on the brain parcellation scheme. Along each axis in such space, the value of the signal in a particular area is stored. Thus, a change in the BOLD-signal of the whole brain can be represented as a movement of a point in this multidimensional space.

In our study, 300 BOLD signal values of 245 ROIs (BN parcels) in increments of 2 s corresponded to 300 functional brain images obtained with TR = 2s, for each scanning session. In other words, there were 300 points in the high-dimensional space in each session. The task was to separate the brain states related to different sessions (RS_0 and RS_FE) as precisely as possible. For this purpose, 300 points from each session were concatenated into a single dataset of 600 points, and class labels were erased. Then the points were divided into two groups employing dimensionality reduction.

2.9. Dimensionality reduction

We used three nonlinear methods for dimensionality reduction: LE (Laplacian eigenmaps), Isomap, LLE (locally linear embedding), and one linear method: PCA (principal component analysis).

We applied PCA on a data matrix of shape 245 × 600 (two concatenated sessions of length 300), transforming it to shape TDx600, where TD is the target dimensionality (number of principal components taken). The proportions of explained variance averaged over all subjects can be found in Fig.S2.

All three nonlinear methods we tested use the construction of the point neighborhood graph in the original space as the first step (see Figs. 1.1–1.3 and comments below). The main focus of our work was on the LE (the justification will be given in the Results section). Therefore, we will now briefly describe the basic steps of Isomap and LLE, and then move on to a detailed description of LE, which will highlight its successful features for our problem.

2.9.1. Isomap

Given the neighborhood graph **G**, Isomap approximates the distance between every two points A and B as a shortest path in the graph A→B. The resulting distance between A and B is a simple sum of distances between successive nearest neighbor pairs. After constructing the full distance matrix, Isomap applies multidimensional scaling (MDS) to it to get the best low-dimensional representation.

2.9.2. Locally linear embedding

Given the neighborhood graph **G**, LLE calculates a set of weights for each point that best describes the point as a linear combination of its neighbors. After that, the weights are "frozen" and the next optimization problem is solved: what should be the coordinates of points in the low-dimensional embedding so that each point is described by the same linear combination of its nearest neighbors as in the original space?

2.9.3. Laplacian eigenmaps

1. The procedure started with a point cloud $\{\boldsymbol{x_i}\}$ lying in high-dimensional space. In our case the number of points $\boldsymbol{N} = 600$, the dimensionality of the original space $\boldsymbol{D} = 245$.
2. We decided not to use the $\boldsymbol{\varepsilon}$-neighborhood method, in which the neighbors of a given point are all those that lie within some predetermined radius $\boldsymbol{\varepsilon}$. Instead, we used the mutual k nearest neighbors algorithm, which tends to form more connected and stable graphs. Thus, the first stage was carried out by building the k nearest neighbors graph. For each point, exactly $\boldsymbol{k}$ nearest ones (in terms of the Euclidean distance) were calculated. After that these neighbors were connected with the given point.
3. Note that the parameter $\boldsymbol{k}$ specifies only the minimum, but not the full number of links for a given node. Each node has exactly $\boldsymbol{k}$ "outgoing" links and theoretically unlimited number of "incoming" links. Note that in Fig. 1.3 ($\boldsymbol{k} = 2$) there are many nodes with degree

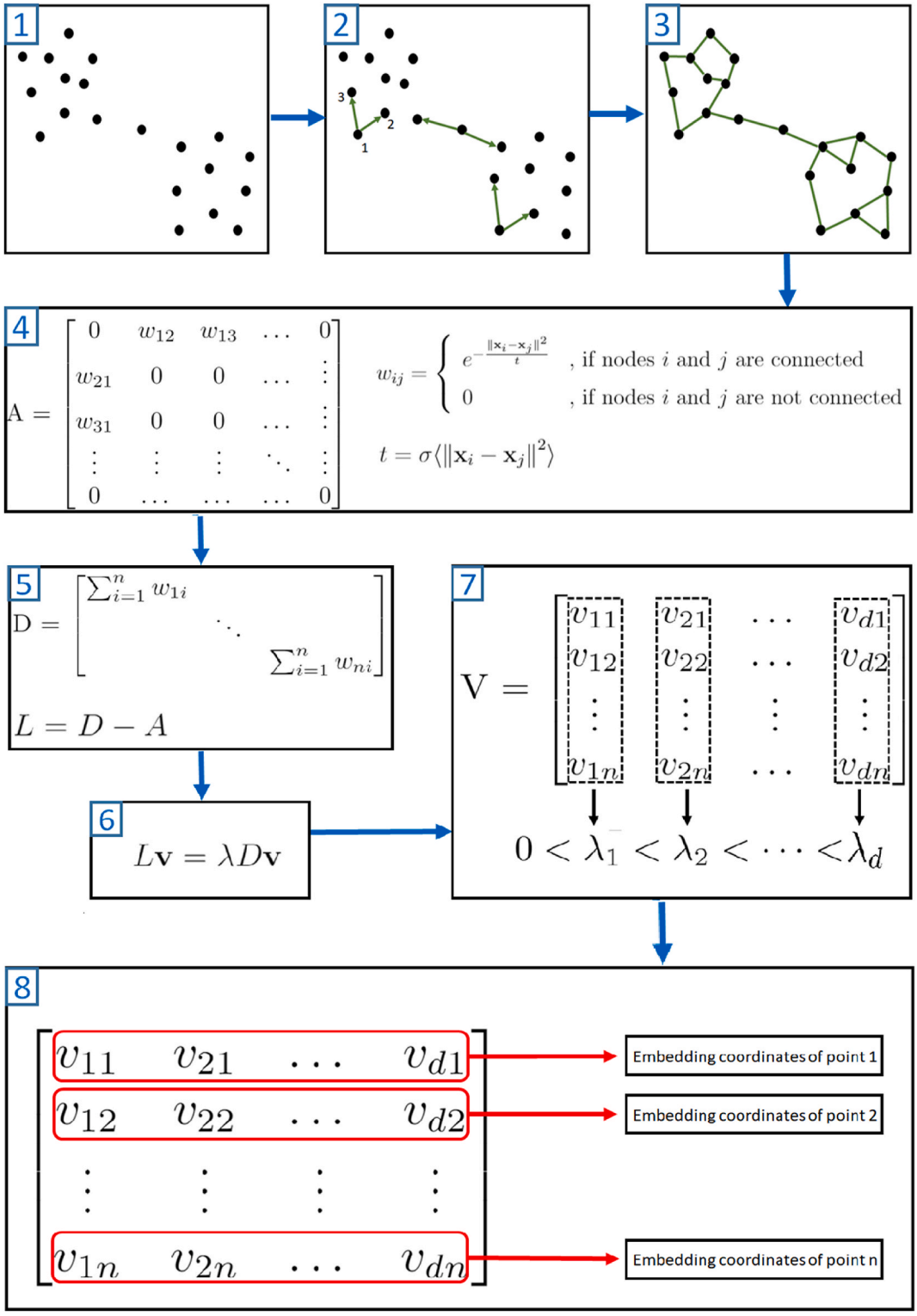

Fig. 1. The steps of Laplacian eigenmaps algorithm. 1–3: Neighborhood graph construction. 4: Building a weighted adjacency matrix. 5: Deriving the degree matrix and graph Laplacian from the adjacency matrix. 6: Solving the generalized eigenvalue problem. 7: The solution contains d<n eigenvectors corresponding to non-zero Laplacian eigenvalues. 8: The components of these eigenvectors are the coordinates of the data points in the reduced d-dimensional space.

>2. The ***k*** parameter was chosen as the minimum possible one to ensure the connectivity of the resulting graph. Such selection preserved the local linearity assumption, which gave sense to the "neighborhood relation" in the initial space.

4. At this stage, the adjacency matrix of the graph was constructed. The resulting neighborhood matrix was made symmetric, in other words, the neighborhood relation was turned to mutual. Each connection in the graph was given its own weight depending on how far apart the points it connects are, according to the formula in Fig. 1.4. Note that the control parameter σ corresponds to the time t in the heat kernel in the original paper (Belkin and Niyogi, 2003), with an accuracy of a constant multiplier equal to the mean square of the distance between

the points in the graph. This small modification was made in order to decouple $\boldsymbol{\sigma}$ from the characteristic distance between points in the graph, to make this parameter dimensionless, and to be able to compare it on the same scale for different graphs. Note that $\boldsymbol{\sigma}\to\infty$ implies the so-called « simple-minded » weighting method which assigns weight 1 to all existing edges in the graph and thus makes the adjacency matrix « binary».

5. Knowing the graph adjacency matrix, we calculated the degree matrix **D** and graph Laplacian **L.**
6. This stage was based on the fact that the solutions of the sparse eigenvalue problem 1.6 are the optimal coordinates for embedding the data in a low-dimensional space (Belkin and Niyogi, 2003). The generalized eigenvalue problem 1.6 can be easily reformulated in terms of eigenvectors of the normalized graph Laplacian.
7. To embed $\boldsymbol{N}$ points in the space of dimensionality $\boldsymbol{d}$, one should take $\boldsymbol{d}$+1 first Laplacian eigenvectors. Each of them has length $\boldsymbol{N}$ equal to the number of nodes in the graph and corresponds to some non-negative eigenvalue in ascending order. The first eigenvector (the so-called principal eigenvector) corresponding to $\lambda = 0$ was not taken into account in the calculations because its components were constant. In case there were several connected components in a graph, the $\lambda = 0$ eigenvalue had the multiplicity equal to the number of separate graph components. However, such cases were excluded due to the condition of graph connectivity from stage 3.
8. The components of these eigenvectors are the new coordinates of data points in low-dimensional space. The Laplacian eigenvectors tend to highlight clusters in the data. For example, the first nontrivial eigenvector will take negative values on points from Fig. 2.3 belonging to the first cluster and positive values on those belonging to the second cluster.

In some experiments we performed dimensionality reduction in two steps. In this case, the coordinates of points in the first embedding became the input data for the second dimensionality reduction. As an intermediate, we chose a dimensionality that roughly coincides with the estimated intrinsic dimensionality of the data (see the next section). The resulting embedding points were then used again to construct the similarity graph and embed them in the space of target dimensionality using the same algorithm. Shuffling of $\boldsymbol{D}$-dimensional activity vectors ($\boldsymbol{D}$=245 stands for the number of ROIs) was not performed as timestamps were not preserved during the construction of a similarity graph. Therefore, the ordering of activity vectors did not affect the final low-dimensional embedding.

The choice of parameters for constructing a graph was dictated by the condition of its connectivity. For the first dimensionality reduction we chose $\mathbf{k_1} = 6$ and $\boldsymbol{\sigma_1} = 1.5$. It is worth noting that the number of nearest neighbors **k** has the main influence on the quality of cluster separation, and $\boldsymbol{\sigma}$ is an additional parameter, which can be used to improve the result. For the second dimensionality reduction, we chose $\mathbf{k_2} = 17$ and $\boldsymbol{\sigma_2}\to\infty$. The choice of such a large number of links at each node was again dictated by connectivity considerations: after the first dimensionality reduction, the points in the embedding were divided into compact groups, and to establish links between these groups, we had to choose $\mathbf{k_2}$ large enough. A detailed analysis of the effect of the graph construction parameters on the quality of separation of the two scanning sessions can be found in Fig.S1. We've studied the values of $\boldsymbol{\sigma_1} \in [1; 5{,}5]$. The values $\boldsymbol{\sigma_1} < 1$ led to "broken" embeddings, since too many edges in the graph were given weights almost equal to zero. Since $\boldsymbol{\sigma_1}$ is in the denominator of the exponent of the Gaussian kernel (see Fig. 1.4), the results for $\boldsymbol{\sigma_1}>5.5$ smoothly converged to the unweighted case ($\boldsymbol{\sigma_1}\to\infty$) and almost stopped changing, thus we are not reporting them.

Since all three manifold learning methods we used rely on graph construction, we used the same values of the parameters $\boldsymbol{k_1}$, $\boldsymbol{k_2}$ for LLE and Isomap. Thus, all methods reused the same graph constructed from the original data.

2.10. Intrinsic dimensionality estimation

To estimate the intrinsic dimensionality of the data, we used several different metrics that best fit the specifics of the methods used.

For Isomap we, following the authors of the original paper (Tenenbaum et al., 2000), calculated the residual variance (RV), a measure of the similarity of the set of pairwise distances between all pairs of points in the original space and in the embedding. It is defined as

$RV = 1 - \rho^2(D_h, D_l)$, where ρ defines the Pearson correlation, elements in D_h and D_l denote the geodesic distances calculated over the graph in the original high-dimensional space and Euclidean distances in the low dimensional embedding respectively. The internal dimensionality is said to coincide with the "elbow point" on the RV vs. dimensionality plot, after which the variance ceases to decrease significantly.

For PCA we report the values of unexplained variance, which is a natural residual error metric for this method.

Finally, for LE and LLE we used the coefficient of variation of **dy/dx** ratio, which is intimately related to a suitable error metric for dimensionality reduction methods that rescale coordinates. The dy-dx method (Demartines and Hérault, 1997) relies on the assumption that a good mapping should preserve as well as possible the proportion between distances in the initial (**dx**) and final (**dy**) spaces. Thus, **dy** should be equal or proportional to **dx**. By the theory of the dy-dx representation, the better the mapping results are, the closer the joint distribution of these two quantities is to a line. To characterize this property quantitatively, the authors of the method (Shi et al., 2009) propose to use the variance of the relation (**dy/dx**) as a measure of dispersion of this quantity from a constant.

Here we slightly modify this measure by looking at the coefficient of variation (CV) instead of variance: $CV = \frac{std(\frac{dy}{dx})}{mean(\frac{dy}{dx})}$. This allows us to make the error metric independent of the degree of rescaling, and also to say more about the distribution of **dy/dx** deviations from constant. For LE method we used all pairs of nearest neighbors to calculate **dy** and **dx**. For LLE, we used root mean-square distances between all nodes and their nearest neighbors (Duan et al., 2013).

The results are presented in Fig. 2. Note that CV values for both LE and LLE are less than 1, which clearly indicates the "thin" tales of the distribution of ratio dy/dx, which decay faster than exponential ones.

You can see that all plots do not have a clear inflection, but we can assume that it is in the area of dimensions 6–10. However, it is obvious that we need a more unambiguous method for determining the intrinsic dimensionality.

Following the method described in Granata et al. (Granata and Carnevale, 2016), we utilized the neighborhood graph **G** itself to estimate the dimensionality of the data without performing any dimensionality reduction. At first, we calculated the geodesic distance matrix just like at the first stage of Isomap algorithm. Then we calculated root mean square deviation (RMSD) between the observed distribution of geodesic distances and the one of a $\boldsymbol{D}$-dimensional hypersphere as a function of $\boldsymbol{D}$. The intrinsic dimensionality can be estimated as the minimal point of this function (see Fig. 3). Such an estimate gives ID = 6.1 ± 0.6.

2.11. Multiscale wavelet transform for smoothing the BOLD signal fluctuations

BOLD-signal has individual variability and non-stationarity. To better distinguish the useful information contained in it, we applied a discrete multiscale wavelet transform (Abry et al., 2002). This method has several advantages over the standard Fourier analysis since wavelet base functions are compactly supported and deal well with non-stationary signals.

Following the published recommendations (Zhang et al., 2016), we selected a wavelet with a sufficiently large number of vanishing moments for the preprocessing step for the main dimensionality reduction

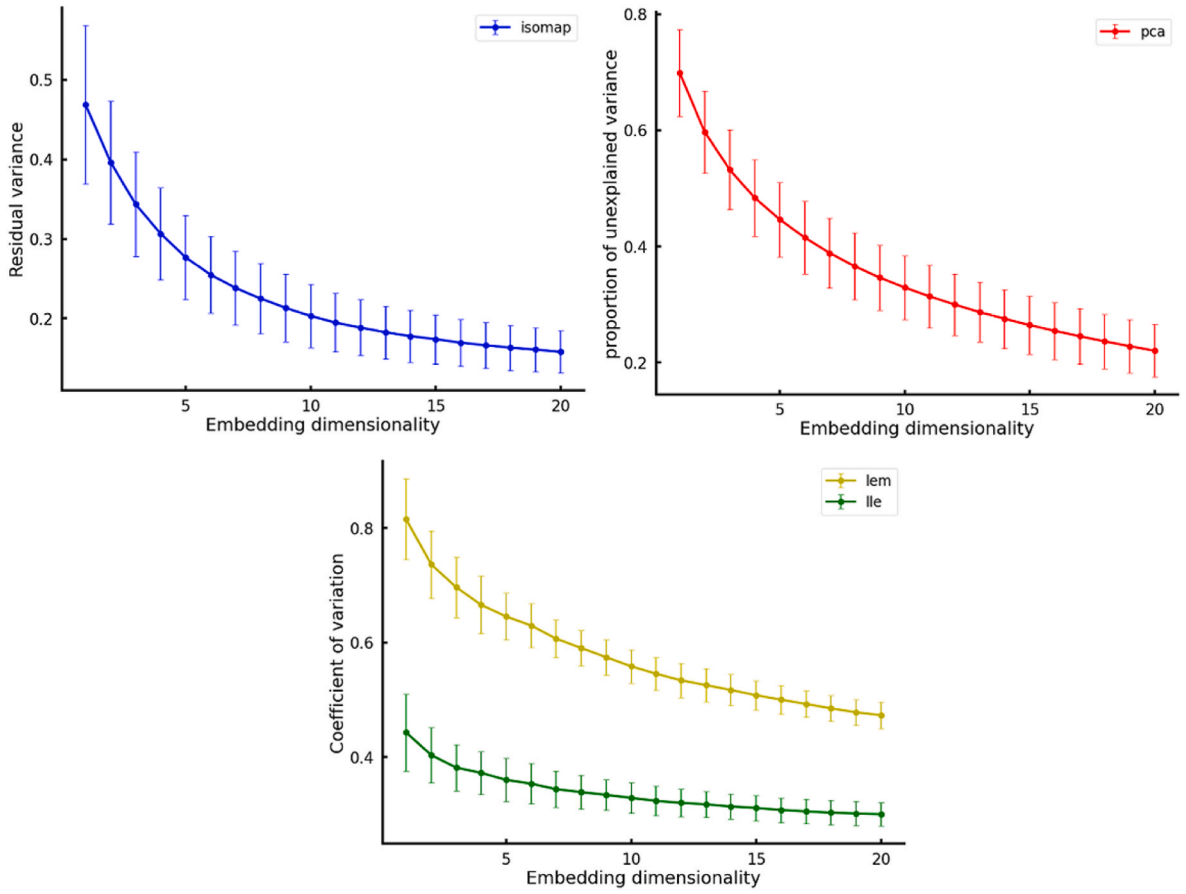

Fig. 2. Error estimations as functions of embedding dimensionality for different manifold learning methods. Bars represent standard deviations.

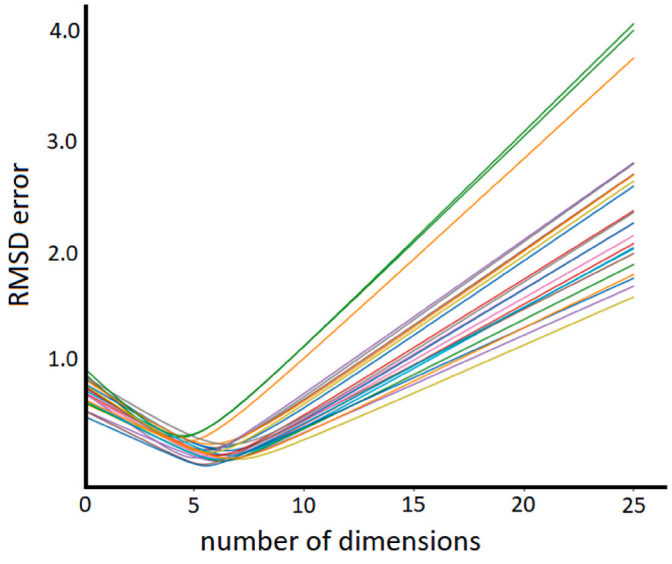

Fig. 3. Root mean square deviation between real and theoretic graph geodesic lengths distribution as a function of internal dimensionality tested. Each line corresponds to one subject.

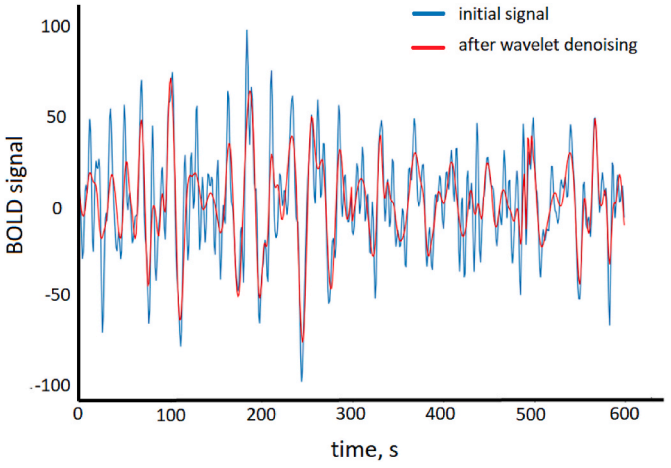

Fig. 4a. An example of an initial (blue) and filtered (red) concatenated BOLD-signal.

results (see Fig. 4a). Detailed justification of our choice will be provided in the Results section. We chose frequently used Daubechies wavelets as well as the so-called "Symlets" for the analysis.

To characterize the discrete wavelet transform (DWT) to which the BOLD signal is subjected, we used two characteristics - the wavelet order (the number of its vanishing moments) and the number of transformation levels. In Fig. 4b we can see the effect of these parameters on the result of the wavelet transform. The more levels in the DWT, the coarser the scale on which the signal is reconstructed. The higher the order of the wavelet, the smoother it becomes.

Multiscale representation provides a hierarchical structure for signal analysis at different "resolutions" and is a natural way of decomposing a signal into several components carrying different aspects of its information content. Such time series representation effectively analyzes the signal's information content with different levels of detail (Mallat, 1989). At each stage of the algorithm, wavelets with a consistently finer

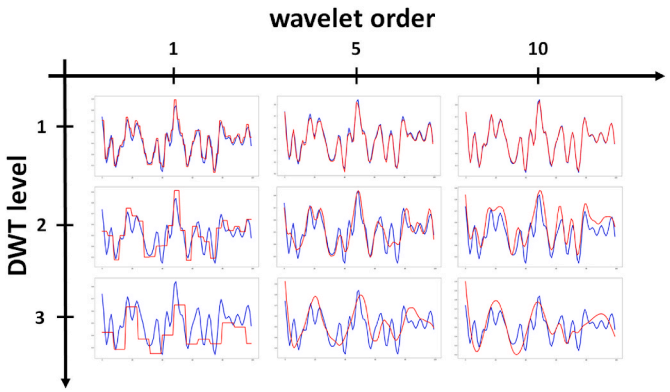

Fig. 4b. The effect of wavelet order (horizontal axes) and number of decomposition levels (vertical axes). Each subplot contains a part of the whole signal of length 100 (blue) and its modified version after applying multiscale wavelet transform (red).

representation of the signal content are generated. Each level of detail represents the signal at a specific resolution.

The first component is a "coarse" version of the signal, which is, in fact, its low-resolution approximation. The other ones are "detail" components that carry information about signal behavior on finer and finer scales, depending on the multiresolution analysis's depth (Mallat, 1989). A variance of detail components on i-th resolution levels estimates the amount of energy concentrated around the i-th scaling frequency.

During the denoising process, the wavelet coefficients that carry information about the "details" of the signal are filtered at each decomposition stage. There are numerous algorithms for selecting such filtration threshold, adapted to different tasks (Luo and Zhang, 2012). After that, filtered detail coefficients are composed again to create a denoised version of an initial signal. The whole process is called "wavelet denoising".

In this work, a relatively simple and universal VisuShrink method was used (Donoho, 1995). It assumes that the noise in the signal is white and is distributed evenly on all characteristic scales. Under such assumptions, it is reasonable to remove all wavelet coefficients smaller than the noise's expected maximum amplitude. This amplitude, in turn, can be estimated from the standard deviation of noise and sample size.

Since the form of the "true signal" (and therefore, the noise) is unknown, our estimate of the standard deviation of noise was based on calculating the median of detailed wavelet coefficients (Mallat, 2009).

The time series used in the numerical experiments were two artificially concatenated sequences of 300 points each (points 0–300 correspond to the first scanning session, points 301–600 correspond to the second one). Therefore, wavelet denoising was performed separately for the first and second half of the combined signal (Fig. 4a). The maximum possible number of levels for DWT was dictated by the length of the signal and in our case was equal to 3.

2.12. Discriminating two resting-state sessions

The ratio of the average distance between points of different classes to the average distance between points of the same class (interclass-intraclass distance, IID) was used as a measure of separation of two classes of points (corresponding to sessions before and after exposure). In this study, we decided to focus on IID analysis because it measures the distance between two populations "in general," which is of interest.

The standard binary classification quality metrics show how well the algorithm handles test data labeling, provided that the class labels for training data are known. We were also interested in another question - how well the data belonging to different scanning sessions were separated in the new low-dimensional space. This is why IID was chosen as the primary metric. Note that if we assign labels to data points randomly, the IID will not exceed 1.01 ± 0.01.

In addition to IID, the accuracy and ROC-AUC score of the k-means clustering algorithm on the embedding data with $k = 10$ was calculated. The results were cross-validated using ten folds (10 non-overlapping train-test data splits, test set contains 10% of data in each split).

All results were averaged over subjects after removing outliers that stood out from the average by more than 2.5 standard deviations.

3. Results

3.1. Comparison of separation accuracy of fMRI data

IID between two sessions after applying PCA was only slightly higher than random: 1.014 ± 0.011 for simple PCA and 1.022 ± 0.015 for PCA with preliminary wavelet denoising. However, wavelet denoising increased accuracy and ROC_AUC score of classification performed on PCA embeddings significantly (see fig. S3 and the next section).

Fig. 5 shows examples of embeddings created by different nonlinear methods. Isomap creates reasonable embeddings and comes right after LE in terms of IID (see Fig. 7, solid lines). The embeddings created by Isomap also have low residual variance (see Fig. 2). This is because during optimization Isomap tries to keep distances between all possible pairs of points, while not being focused explicitly on finding and separating clusters in the data.

As for LLE, it often creates "elongated" embeddings, just like LE. This is a consequence of the temporal structure of the data - points from the "past" find their nearest neighbors in points from the "future", which are separated from them by a short interval, during which the BOLD-signal does not have time to change much. However, the embeddings generated by LLE poorly separate resting-state scanning sessions from each other.

After the dimensionality reduction with the LE algorithm, it was possible to separate the data points belonging to different scanning sessions. For most subjects (19 out of 23), the low-dimensional projection points split up into two clusters corresponding to the sessions before and after fear learning (Fig.6 A and C). The remaining four subjects did not show such discrimination (Fig. 6 B and D), but for all subjects, the IID was significantly higher than a random one.

3.2. Wavelet denoising improves the separation of BOLD signal data from different sessions

After applying a multiscale wavelet transform, shrinking the detail coefficients, and collecting the truncated components back into a time series, we obtained denoised versions of our BOLD signals (see Methods). Applying dimensionality reduction to this new filtered data, we were able to increase IID for the majority of subjects (see Fig. 7) as well as classification metrics (see fig.S3).

Experimenting with different dimensions of the final space, we concluded that a better separation ($IID = 2.2 \pm 0.5$) was achieved when projecting to a line (1D space). In this case applying wavelet preprocessing increased IID by 210% ± 50% for a single dimensionality reduction (dim 245 - > dim 1, see Fig. 7) and by 290% ± 120% for a two-step dimensionality reduction (dim 245 - > dim 10 - > dim 1, see Fig. 10) when compared with the preprocessing-free approach.

Interestingly, applying wavelet preprocessing to the data improved the final result for all dimensionality reduction methods used. Even if we abstract away from the nonlinear nature of the problem at hand, this step led to an increase of the explained variance in dimensionality reduction using PCA (see Fig.S2).

Depending on the parameters of the wavelet transform, its effect on the BOLD signal may be different (see Fig. 4b). We investigated the dependence of IID between two scanning sessions on these parameters, the results are presented in Fig. 8.

Fig. 8 shows that only the wavelet transform with 3 levels of

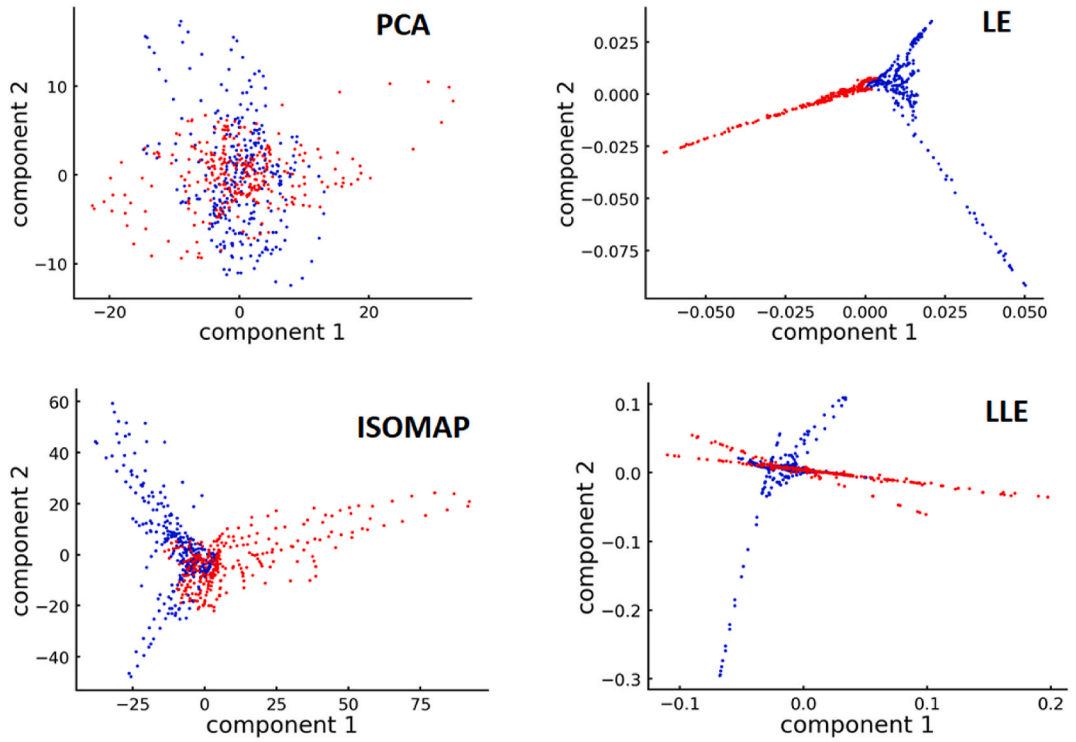

Fig. 5. Two-dimensional embeddings created by different dimensionality reduction methods for the BOLD signal of the same subject. Red and blue points correspond to data from RS_0 and RS_FE sessions respectively. Dimensionality reduction was performed in one step with $\boldsymbol{k} = 6$ for LE, LLE and ISOMAP, $\boldsymbol{\sigma} = 1.5$ for LE.

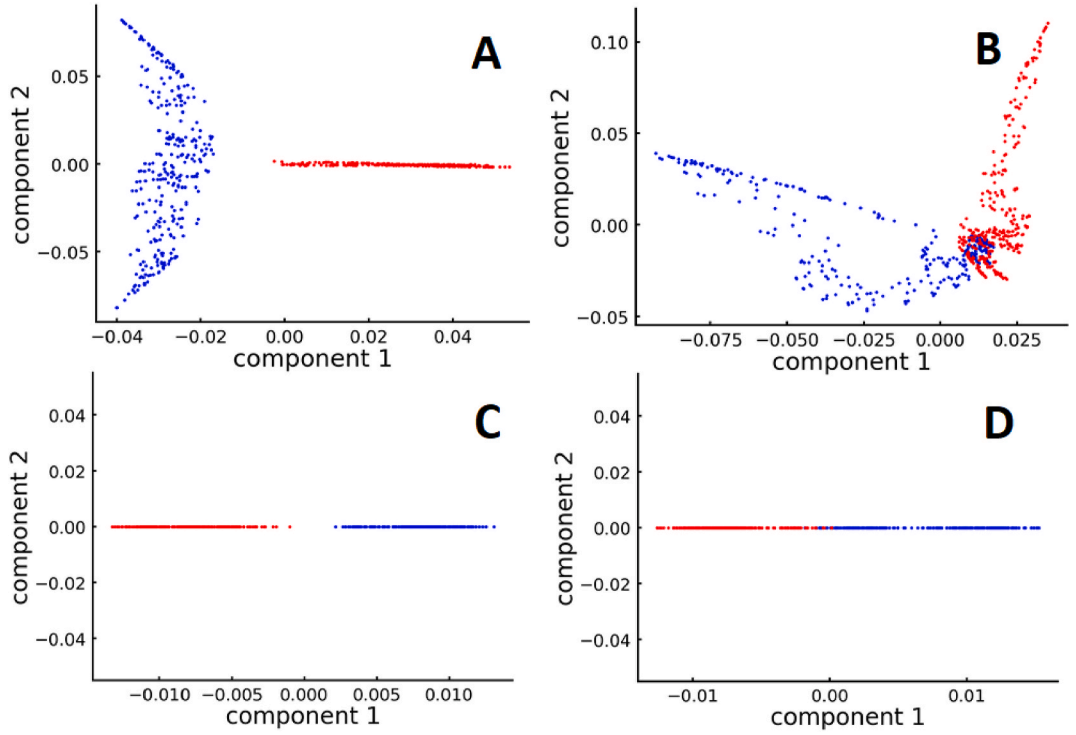

Fig. 6. An example of a "good" (left) and "poor" (right) dimensionality reduction result by means of LE. Red and blue points correspond to data from RS_0 and RS_FE sessions respectively. A, B: two-dimensional projections of data. Parameter values: $\boldsymbol{k_1} = 6$, $\boldsymbol{\sigma_1} = 1.5$. C, D: projections on a one-dimensional line from an intermediate 10-dimensional embedding. Parameter values: $\boldsymbol{k_2} = 17$, $\boldsymbol{\sigma_2} = \infty$. IID values: 8.23 for Fig. 6C and 2.26 for Fig. 6D.

decomposition has a significant effect. The reasons for this can be understood if we analyze the appearance of the proximity graphs in Fig. 9.

The adjacency matrices of these graphs are symmetric since the proximity graphs are undirected. The main diagonal is always empty (self-loops are forbidden). Since our data are time-ordered, and the BOLD-signal changes smoothly, the nearest neighbors of a given point will be separated from it by a small-time interval. This forms side diagonals close to the main one (Fig. 9, bottom).

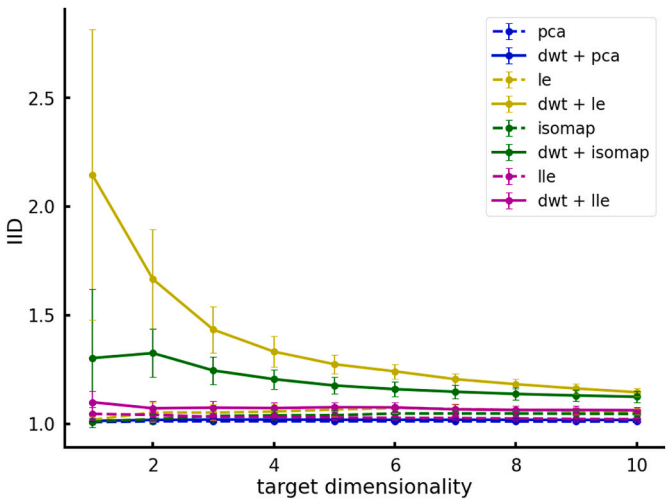

Fig. 7. Improved separation between two RS scanning sessions for different methods before and after applying wavelet denoising (discrete wavelet transform = dwt). Dimensionality was reduced in one step (dim 245 - > target dim). Solid and dashed lines correspond to results with and without applying preliminary wavelet denoising respectively. Bars represent standard deviations. Daubechies 8 wavelet with 3 levels of decomposition was used for the BOLD signal preprocessing.

As noted in Methods, the number of nearest neighbors ***k*** is a minimum bound on the real number of links of a given node. Considering the variability of the BOLD signal, we can see that in a "simple" proximity graph, constructed without signal smoothing, some nodes have a disproportionately large number of links (because they are neighbors to a large number of other nodes). This is reflected in the vertical and horizontal "light bars" in the adjacency matrix (Fig. 9, bottom left). The adjacency matrix of such a graph has too many non-zero elements far from the main diagonal. This makes it impossible to separate the two clusters, because they are too closely intertwined. This line of reasoning is confirmed by the view of the proximity graph (Fig. 9 upper left). Points belonging to the same scanning sessions tend to cluster together. However, this is not enough to separate the data into two classes.

Filtering of the BOLD signal with a wavelet transform smoothes its short-term fluctuations (see Fig. 4a). This causes most of the edges in the graph to connect points that are close to each other in time (Fig. 9 bottom right). However, the "multi-diagonal" structure of the adjacency matrix itself does not yet make it possible to see two clusters: off-diagonal connections play an important role. In contrast to the "simple" graph, in the new adjacency matrix the nonzero off-diagonal elements are located almost entirely in two quadrants (upper left and lower right) corresponding to two scanning sessions. This structure leads to a much more obvious manifestation of clusters (Fig. 9, top right).

This mechanism also explains the effect of the wavelet order. If this parameter is insufficient, the filtered signal turns out too "stepped" (see Fig. 4b) and cannot adequately reflect the neighborhood of two data points in high-dimensional space. If we take this parameter too big, then in the received signal a lot of information will be lost, because it will be too smooth. This will lead to loss of off-diagonal elements in the adjacency matrix of the graph and decrease the quality of separation. As can be seen from Fig. 8, these patterns are common for both types of wavelets considered.

3.3. Preliminary dimensionality reduction by LE algorithm results in a better separation of resting states

A high number of ROIs makes it difficult to find points close to each other in the data because of the so-called "curse of dimensionality". Therefore, usually if the dimensionality of the data is high, it is necessary to first translate it to a space with fewer variables using PCA, and then apply other algorithms. We tried this approach by experimenting with a number of intermediate latent variables ranging from 20 to 40 (this corresponds to a proportion of explained variance of approximately 90%–98%, see Fig.S2). However, none of the three metrics (IID, accuracy, and ROC_AUC) showed significant improvement, and in some cases the results even declined.

Then we decided to replace the linear algorithm (PCA) in the first step with a non-linear algorithm (LE). We used a projection into a 10-dimensional intermediate space. We chose an intermediate dimensionality somewhat larger than the intrinsic dimension of the data to account for the possible loss of useful information in the embedding.

This allowed us to increase the IID between resting-state scanning sessions (see Fig. 10), and also improved the quality of classification for all subsequent non-linear methods and even for PCA (see Fig.S4). Notably, a similar result could not be achieved using other methods for the first dimensionality reduction step.

This effect seems to be due to the peculiarity of LE method, which tries to preserve proximity in a low-dimensional space only for the points connected by edges in the similarity graph. Preliminary reduction

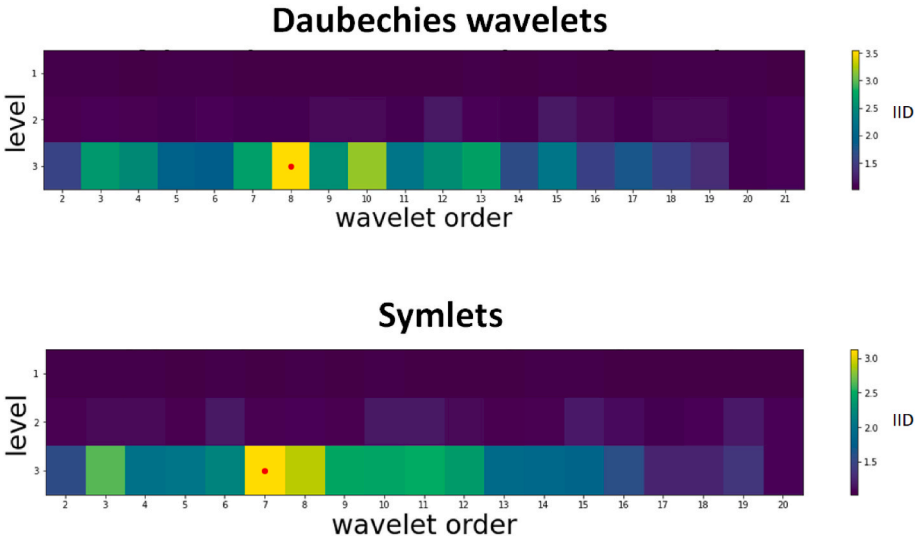

Fig. 8. Dependence of IID on the order of the wavelet used (horizontal axis) and on the number of DWT levels (vertical axis). The IID value is shown in color and corresponds to the color bar on the right. The upper part corresponds to Daubechies wavelets, the lower to symlets.

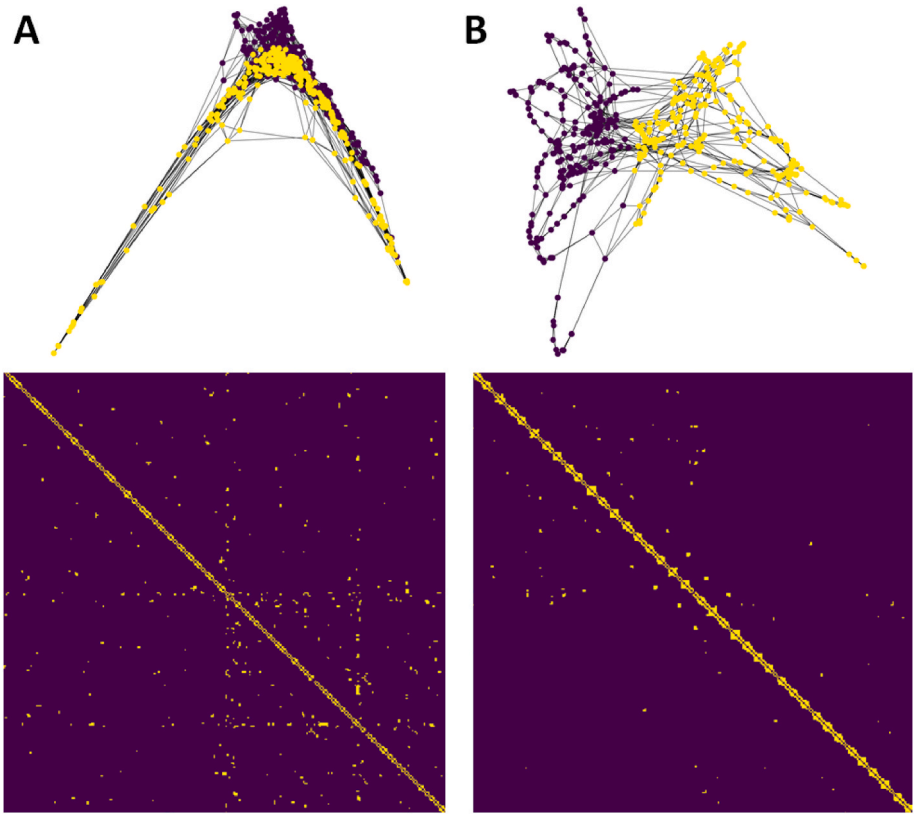

Fig. 9. Effect of the wavelet transform on the shape of the proximity graph. The upper part shows nearest-neighbor graphs (colors indicate that the point belongs to RS_0 or RS_FE session). The lower part shows fragments of adjacency matrices of these graphs. A: the graph built on the original BOLD signal. B: the graph built on the signal after wavelet preprocessing.

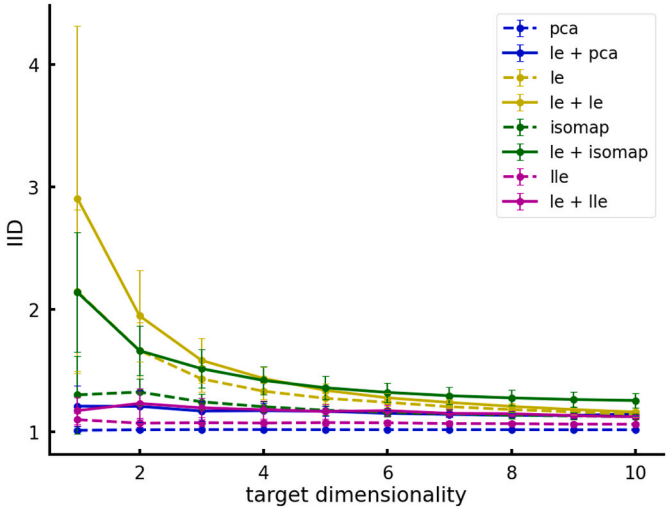

Fig. 10. IID for 1-step dimensionality reduction (245 → target dim, dashed lines) and 2-step dimensionality reduction with first step provided by LE (245 → 10 → target dim, solid lines). depending on the target dimensionality. Bars represent standard deviations. Daubechies 8 wavelet with 3 levels of decomposition was used for the BOLD signal preprocessing.

of dimensionality allows an additional separation of two groups of points belonging to different scanning sessions. This is illustrated in Fig. 11, which shows examples of graphs used for the first and second dimensionality reductions. We can see that the first graph (on the left) retains the "thread" structure characteristic of a set of points belonging to the same signal (since the data have a temporal structure and neighbors "by distance" often turn out to be neighbors "by time"). At the same time, it also has long-range connections, which mean the similarity of the multidimensional BOLD signal at time t_1 to the signal at time t_2, quite far away from t_1. The second graph (on the right) loses this structure, but strongly emphasizes the clusters found in the data.

4. Discussion

Our study aimed to develop a dimensionality reduction method to classify individual differences in BOLD-signal at rest before and after salient stimulus exposure. BOLD-signal values used from the 245 ROIs are not fully independent, and the number of axes required for sufficient data description is significantly lower. However, the interdependencies between the different components of a multidimensional signal can be complex and non-linear. Therefore, we decided to use dimensionality manifold learning methods to identify the data structure in their intrinsic manifold.

For the first time, we show using fMRI data that it is possible to distinguish with high precision brain activity at the level of individual subjects at rest before and after stimulus exposure.

The PCA linear dimensionality reduction method was not successful in this task. Low-dimensional representations returned by linear methods are associated with input vectors of linear transformation features (Belkin and Niyogi, 2003). If the data belong to some linear subspace of the original high-dimensional representation (or are located close to it), the linear methods may create a good embedding into a low-dimensional space. However, they will fail if the data lie on a non-linear manifold because the surface geometry becomes much more complex. Therefore, in this work nonlinear methods were used to restore the internal geometry of data.

The better performance of nonlinear methods could be explained by the nonlinear nature of the BOLD signal. Signal fluctuations are essential

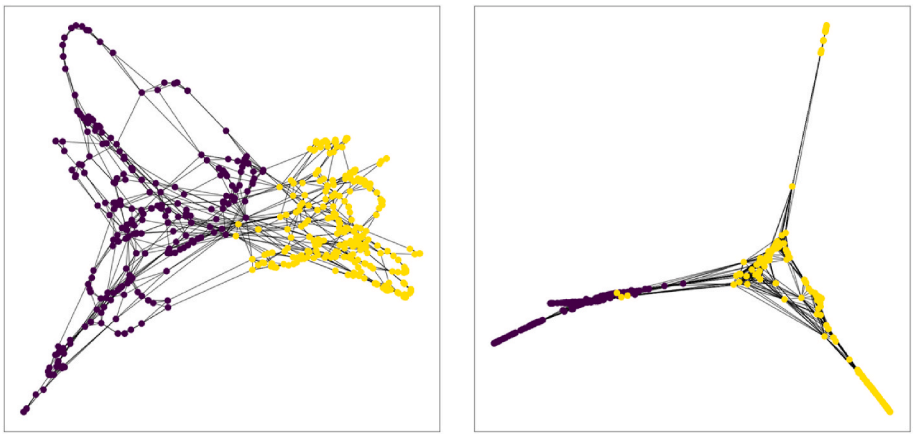

Fig. 11. Comparison of k-nearest neighbors proximity graphs obtained for a single subject during the first (left) and second (right) dimensionality reduction steps. Left part: $k_1 = 6$, $\sigma_1 = 1.5$. Right part: $k_2 = 17$, $\sigma_2 = \infty$. Point coordinates are given by projecting the LE embedding on a 2-dimensional plane. Colors indicate that the point belongs to RS_0 or RS_FE session.

for maintaining the optimal state of brain activity and for flexibility between states (Tognoli and Kelso, 2014; McIntosh et al., 2010). We have also demonstrated at the same data set that fractality of fMRI signal in two resting states before and after fear learning and extinction were different at the group level in the specific brain areas related to fear-processing (Tetereva et al., 2020). However, at the individual level, conventional statistic comparison of fractality (measured by detrend fluctuation analysis) could not provide unambiguous results for all subject data in our dataset.

When choosing a dimensionality reduction algorithm, we were guided first of all by its ability to restore the "internal manifold" of our data. However, it is important to keep in mind that each dimensionality reduction method focuses on different aspects of manifold reproduction in low-dimensional space. For example, Isomap takes into account all possible pairwise distances between data points. LLE, on the other hand, focuses on reconstructing each point as a linear combination of its neighbors. In our task of separating two resting-state scanning sessions, the LE method worked best. This is expected, since LE tends to keep the pairwise distances only between neighboring points in the embedding, and ignores all others. This leads to compact clusters reflecting groups of similar elements in the data (in our case, the BOLD signal values in the first and second scanning sessions). LE's significant advantage is a clear geometric meaning of the reduced space coordinates - their ability to dictate the optimal division of the graph into non-intersecting clusters (Shi and Malik, 2000).

Our task was not just to develop a classifier that would distinguish data from the first and the second sessions. We wanted to build a low-dimensional embedding of the data that would naturally separate the two data groups. Therefore, we focused on the manifold learning algorithms. This approach was successfully adopted in recent papers: the local linear embedding algorithm served as a useful feature extraction procedure that helped to recognize psychiatric disorders (Sidhu, 2019). Manifold discovery using LE was performed on fMRI images (Thirion and Faugeras, 2004). Being applied to fMRI images, this technique facilitated the discrimination of structures of interest. Manifold learning methods have been applied to functional brain networks (Qiu et al., 2015) to construct optimal low-dimensional embeddings.

BOLD signal preprocessing through wavelet denoising helped to improve the separation of two data groups significantly. The best wavelet we tested was Daubechies 8 (see Fig. 8). We suggest this is due to its resemblance to the characteristic form of a BOLD signal, as well as to the high enough number of vanishing moments (Zhang et al., 2016).

The optimal number of levels (n) for multiresolution analysis was 3: this seems to be because with $n \leq 2$ the BOLD-signal was not filtered on a large scale. The frequency range often interpreted in resting fMRI is 0.008–0.15Hz (Zhang et al., 2016). In our case, we used a band-pass filter of 0.01–0.1 Hz. Scanning was performed with TR = 2s; thus, scale 2 coefficients correspond to the range 0.025–0.05 Hz, and scale 3 coefficients correspond to the range 0.0125–0.025 Hz. It seems that the wavelet coefficients in these two frequency bands are essential for separating brain states before and after exposure.

We should clarify the relationship between the role of wavelet preprocessing and manifold learning methods in our analysis. Fig. 7 clearly shows that without applying wavelet preprocessing, the results in terms of IID are poor. At the same time, Fig.S2 and Fig.S3 show that the nonlinear manifold learning methods handle the classification of resting state sessions significantly better than PCA, even without wavelets. However, the advantages of LE over other manifold learning methods become fully apparent in combination with wavelet preprocessing (we explore the reasons for this in the Results section "Wavelet denoising improves the separation of BOLD signal data from different sessions," see Fig. 9). Therefore, it is important to emphasize that for our analysis, both the choice of method and the correct preprocessing of the BOLD signal are important.

Our results imply the following sequence, in which each successive dimensionality reduction variant yields a better result than the previous one (both in terms of IID and in terms of classification quality metrics):

1. PCA
2. LE, LLE, Isomap
3. LLE, Isomap + wavelet preprocessing
4. LE + wavelet preprocessing.

In addition, we show that the use of LE as a dimensionality reduction preprocessing method improves the results for all methods considered, which is not the case for all other methods (see Fig. 10). Again, we believe this is because LE creates a suboptimal 2-cluster embedding during the first dimensionality reduction, which is easier to be processed by other methods during the second step (see Fig. 11).

An important issue when reducing the dimensionality of data is the optimal number of axes of the embedding. In this study, we found that for all subjects, the internal dimensionality of the original 245-dimensional data ranges from 6 to 10. This finding is most likely associated with the high degree of correlation between BOLD signals in different brain regions. In the future, analysis of these several non-linear components may shed light on the integration processes in the brain and the architecture of its functional networks.

The best separation of data from two sessions was obtained in a 1D projection. In this case, the only coordinate specifying the position of a point on the line is the component of the first nontrivial Laplacian

eigenvector (the so-called Fiedler vector), which is responsible for cutting the graph into two optimal halves (Shi and Malik, 2000).

This fact can also be interpreted in terms of the Diffusion maps algorithm. It is known that the low-dimensional representations returned by this method coincide with the LE embeddings for diffusion time $t = 0$. In the general case Diffusion maps returns the same coordinates as LE, but "stretched" according to the importance of the eigenvectors of the Laplacian, which is given by the corresponding eigenvalue. The larger the diffusion time parameter t, the greater the role of the very first eigenvectors. In the $t \to \infty$ limit, only the Fiedler vector, which captures large-scale structures in the data, remains from the whole multivariate picture.

However, this does not mean that the data can be well described with a single variable. Instead, we have revealed the meaning of only one, albeit the most important, coordinate axis in the latent space. The meaning of the other variables remains to be identified. One of the possible ways for physiological interpretation of the latent variables could be provided by correlating them with behavioral metrics. Previously, we tested correlations with behavioral (State and Trait anxiety) and physiological (skin conductance response during fear extinction procedure) measures with an event-related BOLD response and functional connectivity of the amygdala (Martynova et al., 2020). Despite our expectations, we did not find significant correlations. In this study we could not obtain significant correlations as well, possibly due to correction for multiple comparisons and relatively small sample size, which also limits the current study findings. Further research on larger data samples is needed to find a substantial relationship between observed behavioral indices and obtained variables after fMRI data dimensionality reduction.

Our findings are consistent with the previous data (Bahrami et al., 2019; Hong et al., 2020; Billings et al., 2017), the main difference being a successful application of the LE dimensionality reduction to separate the brain RS activity before and after meaningful stimulus exposure. In the previous studies, using a conventional fMRI analysis we also showed that functional connectivity of the amygdala differed significantly before and after fear learning and exposure in the resting state condition at the group level (Martynova et al., 2020). In this study, we demonstrate the supplementary approach to separate data on brain activity with good accuracy at the individual level.

As a limitation of the present results, we should mention that one of the main problems of manifold learning methods is the interpretation of latent space axes, which is often done empirically, without any initial hypothesis. Hence, the further progress on "mapping" the space of hidden variables (Liu et al., 2019) is critical. Future research should explore different interpretation strategies of latent space components resulting in better recognition accuracy using free-shared fMRI datasets. Such interpretation should provide a better understanding of neurophysiological processes underpinning exposure-induced changes in the brain resting-state dynamic.

5. Conclusions

Our study demonstrated that the Laplacian eigenmaps manifold learning method applied to fMRI data could reveal differences between the RS functional brain activity before and after exposure of subject to a salient stimulus. Our findings also demonstrate that RS functional brain networks retain effects of stimuli exposure even after a time lag.

Author contributions

Those who conceived and designed the study include NP, AT, OM and KA. AT performed the experiments. AT and NP analyzed the data. NP and OM wrote the paper.

Funding

This study was supported by the Ministry of Science and Higher Education of the Russian Federation grant No. 075-15-2020-801, and partially within the state assignment of the Ministry of Science and Higher Education of the Russian Federation for IHNA&NPh RAS.

Declaration of competing interest

The authors declare that they have no known competing financial interests or personal relationships that could have appeared to influence the work reported in this paper.

Acknowledgements

We are grateful to Dr. S. Nechaev and Dr. A. Gorsky for important suggestions and comments on the manuscript.

Appendix A. Supplementary data

Supplementary data to this article can be found online at https://doi.org/10.1016/j.ynirp.2021.100035.

References

Abry, P., Baraniuk, R., Flandrin, P., Riedi, R., Veitch, D., 2002. Multiscale nature of network traffic. IEEE Signal Process. Mag. https://doi.org/10.1109/79.998080.

Baeken, C., Marinazzo, D., Van Schuerbeek, P., et al., 2014. Left and right amygdala - mediofrontal cortical functional connectivity is differentially modulated by harm avoidance. PloS One. https://doi.org/10.1371/journal.pone.0095740.

Bahrami, M., Lyday, R.G., Casanova, R., Burdette, J.H., Simpson, S.L., Laurienti, P.J., 2019. Using low-dimensional manifolds to map relationships between dynamic brain networks. Front. Hum. Neurosci. https://doi.org/10.3389/fnhum.2019.00430.

Barch, D.M., 2017. Resting-state functional connectivity in the human connectome project: current status and relevance to understanding psychopathology. Harv. Rev. Psychiatr. https://doi.org/10.1097/HRP.0000000000000166.

Belkin, M., Niyogi, P., 2003. Laplacian eigenmaps for dimensionality reduction and data representation. Neural Comput. https://doi.org/10.1162/089976603321780317.

Belleau, E.L., Pedersen, W.S., Miskovich, T.A., Helmstetter, F.J., Larson, C.L., 2018. Cortico-limbic connectivity changes following fear extinction and relationships with trait anxiety. Soc. Cognit. Affect Neurosci. https://doi.org/10.1093/scan/nsy073.

Billings, J.C.W., Medda, A., Shakil, S., et al., 2017. Instantaneous brain dynamics mapped to a continuous state space. Neuroimage. https://doi.org/10.1016/j.neuroimage.2017.08.042.

Brown, V.M., Labar, K.S., Haswell, C.C., et al., 2014. Altered resting-state functional connectivity of basolateral and centromedial amygdala complexes in posttraumatic stress disorder. Neuropsychopharmacology. https://doi.org/10.1038/npp.2013.197.

Coifman, R.R., Lafon, S., 2006. Diffusion maps. Appl. Comput. Harmon. Anal. https://doi.org/10.1016/j.acha.2006.04.006.

Demartines, P., Hérault, J., 1997. Curvilinear component analysis: a self-organizing neural network for nonlinear mapping of data sets. IEEE Trans. Neural Network. https://doi.org/10.1109/72.554199.

Donoho, D.L., 1995. De-noising by soft-thresholding. IEEE Trans. Inf. Theor. https://doi.org/10.1109/18.382009.

Duan, M., Fan, J., Li, M., Han, L., Huo, S., 2013. Evaluation of dimensionality-reduction methods from peptide folding-unfolding simulations. J. Chem. Theor. Comput. https://doi.org/10.1021/ct400052y.

Fan, L., Li, H., Zhuo, J., et al., 2016. The human brainnetome Atlas: a new brain Atlas based on connectional architecture. Cerebr. Cortex. https://doi.org/10.1093/cercor/bhw157.

Fristen, K.J., Frith, C.D., Fletcher, P., Liddle, P.F., Frackowiak, R.S.J., 1996. Functional topography: multidimensional scaling and functional connectivity in the brain. Cerebr. Cortex. https://doi.org/10.1093/cercor/6.2.156.

Gallos, I., Siettos, C., 2017. Classification of fMRI resting-state maps using machine learning techniques: a comparative study. In: AIP Conference Proceedings. https://doi.org/10.1063/1.5012477.

Gallos, I.K., Gkiatis, K., Matsopoulos, G.K., Siettos, C., 2021. ISOMAP and machine learning algorithms for the construction of embedded functional connectivity networks of anatomically separated brain regions fromresting state fMRI data of patients with Schizophrenia. AIMS Neurosci. https://doi.org/10.3934/Neuroscience.2021016.

Graham, B.M., Milad, M.R., 2011. The study of fear extinction: implications for anxiety disorders. Am. J. Psychiatr. https://doi.org/10.1176/appi.ajp.2011.11040557.

Granata, D., Carnevale, V., 2016. Accurate estimation of the intrinsic dimension using graph distances: unraveling the geometric complexity of datasets. Sci. Rep. https://doi.org/10.1038/srep31377.

Griffanti, L., Salimi-Khorshidi, G., Beckmann, C.F., et al., 2014. ICA-based artefact removal and accelerated fMRI acquisition for improved resting state network imaging. Neuroimage. https://doi.org/10.1016/j.neuroimage.2014.03.034.
Hahn, A., Stein, P., Windischberger, C., et al., 2011. Reduced resting-state functional connectivity between amygdala and orbitofrontal cortex in social anxiety disorder. Neuroimage. https://doi.org/10.1016/j.neuroimage.2011.02.064.
Harrison, L.M., Penny, W., Daunizeau, J., Friston, K.J., 2008. Diffusion-based spatial priors for functional magnetic resonance images. Neuroimage. https://doi.org/10.1016/j.neuroimage.2008.02.005.
Hohenfeld, C., Werner, C.J., Reetz, K., 2018. Resting-state connectivity in neurodegenerative disorders: is there potential for an imaging biomarker? NeuroImage Clin. https://doi.org/10.1016/j.nicl.2018.03.013.
Hong, S.J., Xu, T., Nikolaidis, A., et al., 2020. Toward a connectivity gradient-based framework for reproducible biomarker discovery. Neuroimage. https://doi.org/10.1016/j.neuroimage.2020.117322.
Hu, C., Sepulcre, J., Johnson, K.A., Fakhri, G.E., Lu, Y.M., Li, Q., 2016. Matched signal detection on graphs: theory and application to brain imaging data classification. Neuroimage. https://doi.org/10.1016/j.neuroimage.2015.10.026.
Jenkinson, M., Bannister, P., Brady, M., Smith, S., 2002. Improved optimization for the robust and accurate linear registration and motion correction of brain images. Neuroimage. https://doi.org/10.1016/S1053-8119(02)91132-8.
Jung, Y.H., Shin, J.E., Lee, Y.I., Jang, J.H., Jo, H.J., Choi, S.H., 2018. Altered amygdala resting-state functional connectivity and hemispheric asymmetry in patients with social anxiety disorder. Front. Psychiatr. https://doi.org/10.3389/fpsyt.2018.00164.
Khosla, M., Jamison, K., Ngo, G.H., Kuceyeski, A., Sabuncu, M.R., 2019. Machine learning in resting-state fMRI analysis. Magn. Reson. Imaging. https://doi.org/10.1016/j.mri.2019.05.031.
Kim, M.J., Gee, D.G., Loucks, R.A., Davis, F.C., Whalen, P.J., 2011. Anxiety Dissociates dorsal and ventral medial prefrontal cortex functional connectivity with the amygdala at rest. Cerebr. Cortex. https://doi.org/10.1093/cercor/bhq237.
Liu, C., JaJa, J., Pessoa, L., 2018. LEICA: laplacian eigenmaps for group ICA decomposition of fMRI data. Neuroimage. https://doi.org/10.1016/j.neuroimage.2017.12.018.
Liu, Y., Jun, E., Li, Q., Heer, J., 2019. Latent space cartography: visual analysis of vector space embeddings. Comput. Graph. Forum. https://doi.org/10.1111/cgf.13672.
Luo, G., Zhang, D., 2012. Wavelet denoising. In: Advances in Wavelet Theory and Their Applications in Engineering. Physics and Technology. https://doi.org/10.5772/37424.
Mallat, S.G., 1989. A theory for multiresolution signal decomposition: the wavelet representation. IEEE Trans. Pattern Anal. Mach. Intell. https://doi.org/10.1109/34.192463.
Mallat, S., 2009. A Wavelet Tour of Signal Processing. https://doi.org/10.1016/B978-0-12-374370-1.X0001-8.
Mannfolk, P., Wirestam, R., Nilsson, M., Ståhlberg, F., Olsrud, J., 2010. Dimensionality reduction of fMRI time series data using locally linear embedding. Magn Reson Mater Physics, Biol Med. https://doi.org/10.1007/s10334-010-0204-0.
Martynova, O.V., Sushinskaya-Tetereva, A.O., Balaev, V.V., Ivanitskii, A.M., 2017. Correlation between the functional connectivity of brain areas active in the resting state with behavioral and psychological indicators. Neurosci. Behav. Physiol. https://doi.org/10.1007/s11055-017-0520-1.
Martynova, O., Tetereva, A., Balaev, V., Portnova, G., Ushakov, V., Ivanitsky, A., 2020. Longitudinal changes of resting-state functional connectivity of amygdala following fear learning and extinction. Int. J. Psychophysiol. https://doi.org/10.1016/j.ijpsycho.2020.01.002.
McInnes, L., Healy, J., Saul, N., Großberger, L., 2018. UMAP: uniform manifold approximation and projection. J Open Source Softw. https://doi.org/10.21105/joss.00861.
McIntosh, A.R., Kovacevic, N., Lippe, S., Garrett, D., Grady, C., Jirsa, V., 2010. The development of a noisy brain. Arch. Ital. Biol. https://doi.org/10.4449/aib.v148i3.1225.
Poldrack, R.A., Fletcher, P.C., Henson, R.N., Worsley, K.J., Brett, M., Nichols, T.E., 2008. Guidelines for reporting an fMRI study. Neuroimage. https://doi.org/10.1016/j.neuroimage.2007.11.048.
Prater, K.E., Hosanagar, A., Klumpp, H., Angstadt, M., Phan, K.L., 2013. Aberrant amygdala-frontal cortex connectivity during perception of fearful faces and at rest in generalized social anxiety disorder. Depress. Anxiety. https://doi.org/10.1002/da.22014.
Pruim, R.H.R., Mennes, M., van Rooij, D., Llera, A., Buitelaar, J.K., Beckmann, C.F., 2015. ICA-AROMA: a robust ICA-based strategy for removing motion artifacts from fMRI data. Neuroimage. https://doi.org/10.1016/j.neuroimage.2015.02.064.
Qiu, A., Lee, A., Tan, M., Chung, M.K., 2015. Manifold learning on brain functional networks in aging. Med. Image Anal. https://doi.org/10.1016/j.media.2014.10.006.
Rubin, A., Sheintuch, L., Brande-Eilat, N., et al., 2019. Revealing neural correlates of behavior without behavioral measurements. Nat. Commun. https://doi.org/10.1038/s41467-019-12724-2.
Rus, O.G., Reess, T.J., Wagner, G., Zimmer, C., Zaudig, M., Koch, K., 2017. Functional and structural connectivity of the amygdala in obsessive-compulsive disorder. NeuroImage Clin. https://doi.org/10.1016/j.nicl.2016.12.007.
Satterthwaite, T.D., Baker, J.T., 2015. How can studies of resting-state functional connectivity help us understand psychosis as a disorder of brain development? Curr. Opin. Neurobiol. https://doi.org/10.1016/j.conb.2014.10.005.
Sheffield, J.M., Barch, D.M., 2016. Cognition and resting-state functional connectivity in schizophrenia. Neurosci. Biobehav. Rev. https://doi.org/10.1016/j.neubiorev.2015.12.007.
Shen, X., Meyer, F.G., 2005. Analysis of event-related fMRI data using diffusion maps. Inf. Process Med. Imaging.
Shi, J., Malik, J., 2000. Normalized cuts and image segmentation. IEEE Trans. Pattern Anal. Mach. Intell. https://doi.org/10.1109/34.868688.
Shi, L., Yang, Q., Xu, Y., He, P., 2009. A model of selecting the parameters based on the variance of distance ratios for manifold learning algorithms. In: 6th International Conference on Fuzzy Systems and Knowledge Discovery, FSKD 2009. https://doi.org/10.1109/FSKD.2009.471.
Sidhu, G., 2019. Locally linear embedding and fMRI feature selection in psychiatric classification. IEEE J Transl Eng Heal Med. https://doi.org/10.1109/JTEHM.2019.2936348.
Sun, G., Zhang, S., Zhang, Y., et al., 2019. Effective dimensionality reduction for visualizing neural dynamics by laplacian eigenmaps. Neural Comput. https://doi.org/10.1162/neco_a_01203.
Tenenbaum, J.B., De Silva, V., Langford, J.C., 2000. A global geometric framework for nonlinear dimensionality reduction. Science 84. https://doi.org/10.1126/science.290.5500.2319.
Tetereva, A., Kartashov, S., Ivanitsky, A., Martynova, O., 2020. Variance and scale-free properties of resting-state blood oxygenation level-dependent signal after fear memory acquisition and extinction. Front. Hum. Neurosci. https://doi.org/10.3389/fnhum.2020.509075.
Thirion, B., Faugeras, O., 2004. Nonlinear dimension reduction of fMri data: the laplacian embedding approach. In: 2004 2nd IEEE International Symposium on Biomedical Imaging: Macro to Nano. https://doi.org/10.1109/isbi.2004.1398552.
Tognoli, E., Kelso, J.A.S., 2014. The metastable brain. Neuron. https://doi.org/10.1016/j.neuron.2013.12.022.
van den Heuvel, M.P., Hulshoff Pol, H.E., 2010. Exploring the brain network: a review on resting-state fMRI functional connectivity. Eur. Neuropsychopharmacol. https://doi.org/10.1016/j.euroneuro.2010.03.008.
Van Der Maaten, L., Hinton, G., 2008. Visualizing data using t-SNE. J. Mach. Learn. Res.
Zhang, Z., Telesford, Q.K., Giusti, C., Lim, K.O., Bassett, D.S., 2016. Choosing wavelet methods, filters, and lengths for functional brain network construction. PloS One. https://doi.org/10.1371/journal.pone.0157243.
Zhou, Y., Wang, Z., Qin, L di, et al., 2012. Early altered resting-state functional connectivity predicts the severity of post-traumatic stress disorder symptoms in acutely traumatized subjects. PloS One. https://doi.org/10.1371/journal.pone.0046833.